HHS Public Access

Author manuscript

*Neuroimage*. Author manuscript; available in PMC 2022 October 20.

Published in final edited form as:

*Neuroimage*. 2021 November 15; 242: 118434. doi:10.1016/j.neuroimage.2021.118434.

# High-sensitivity detection of optogenetically-induced neural activity with functional ultrasound imaging

**Bradley Jay Edelman**[1], **Giovanna D. Ielacqua**[1], **Russell W. Chan**[1], **Mazen Asaad**[1,2], **Mankin Choy**[1], **Jin Hyung Lee**[1,3,4,5,6,*]

[1]Department of Neurology and Neurological Sciences, Stanford University, Stanford, CA 94305, USA

[2]Department of Molecular and Cellular Physiology, Stanford University, Stanford, CA 94305, USA

[3]Department of Bioengineering, Stanford University, Stanford, CA 94305, USA

[4]Department of Electrical Engineering, Stanford University, CA 94305, USA

[5]Department of Neurosurgery, Stanford University, Stanford, CA 94305, USA

[6]Lead Contact

## Abstract

Whole-brain imaging approaches and optogenetic manipulations are powerful tools to map brain-wide neural circuits in vivo. To date, functional magnetic resonance imaging (fMRI) provides the most comprehensive evaluation of such large-scale circuitry. However, functional ultrasound imaging (fUSI) has recently emerged as a complementary imaging modality that can extend such measurements towards the context of diverse behavioral states and tasks. Nevertheless, in order to properly interpret the fUSI signal during these complicated scenarios, it must first be carefully validated against well-established technologies, such as fMRI, in highly controlled experimental settings. Here, to address this need, we compared subsequent fMRI and fUSI recordings in response to direct neuronal activation via optogenetics in the same animals under an identical anesthetic protocol. Specifically, we applied various intensities of light stimulation to the primary motor cortex (M1) of mice and compared the spatiotemporal dynamics of the elicited fMRI and fUSI signals. Overall, our general linear model analysis (t-scores) and time series analysis (z-scores) revealed that fUSI was more sensitive than fMRI for detecting optogenetically-induced neuronal activation. Local field potential recordings in the bilateral M1 and striatum also better co-localized with fUSI activation patterns than those of fMRI. Finally, the fUSI response contained distinct arterial and venous components that provide vascular readouts of neuronal activity with vessel-type specificity.

[*]**Corresponding Author and Lead Contact**: Jin Hyung Lee, PhD, ljinhy@stanford.edu, 318 Campus Drive, #W300A, Stanford, CA 94305.

CRediT Authorship Contributions

**Bradley Jay Edelman**: Conceptualization, Methodology, Software, Validation, Formal Analysis, Investigation, Resources, Data Curation, Writing – Original Draft, Writing – Review & Editing, Visualization, Project Administration. **Giovanna D. Ielacqua**: Investigation, Resources. **Russell W. Chan**: Investigation, Resources. **Mazen Asaad**: Software. **Mankin Choy**: Conceptualization, Software. **Jin Hyung Lee**: Conceptualization, Writing – Review & Editing, Supervision, Project Administration, Funding Acquisition.

Declaration of Competing Interests

JHL is a founder, shareholder, and consultant for LVIS.

**Keywords**

functional ultrasound imaging; functional magnetic resonance imaging; optogenetics; neural circuits; motor cortex

## 1. Introduction

Functional ultrasound imaging (fUSI) is a promising technology for studying large-scale neural dynamics with high spatial-temporal resolution (Brunner et al., 2020; Macé et al., 2011, 2018; Rabut et al., 2019; Urban et al., 2015). This technique is based on insonifying biological tissue at ultrafast frame rates to measure the power Doppler (PD) hemodynamic signal that proportional to cerebral blood volume (CBV) (Macé et al., 2011; Rubin et al., 1994). Ultrafast imaging reconstructs a full ultrasound image based on the echoes produced by a single plane-wave emission using software beamforming. This approach is attractive as it can be used to excite biological tissue much faster (up to ~40 kHz) than traditional beam scanning (up to ~300 Hz). The combination of ultrafast imaging and coherent compounding (a form of synthetic focusing that combines plane waves from multiple angles) for PD imaging dramatically reduces noise and increases sensitivity by a factor of nearly 50 (Mace et al., 2013; Macé et al., 2011). When ultrasound images are acquired at a sampling rate on the order of hundreds of Hz, the Doppler shift of red blood cells (RBCs) moving within the cerebral vasculature can be indirectly detected. This is done by examining the phase shift of the echo signal in each voxel (termed the Doppler signal) that is generated over the course of hundreds of images. While RBC velocity and direction can be inferred from this information by examining individual frequency components of the Doppler spectrum, the integral of this spectrum correlates with the CBV. Therefore, collecting multiple PD frames in succession provides a time-resolved hemodynamic readout of brain activity.

For the past few decades, functional magnetic resonance imaging (fMRI) has been the standard for measuring brain-wide hemodynamic activity. In recent years, fMRI has also uniquely enabled cell-type specific investigation of brain-wide neural circuits with the aid of optogenetic stimulation (Lee et al., 2010). Exemplary work identifying and dissecting global brain networks underlying neurological diseases such as Parkinson's disease and epilepsy has demonstrated the utility of this approach (Bernal-Casas et al., 2017; Duffy et al., 2020; Lee et al., 2016; Liu et al., 2015; Weitz et al., 2019). Even though fMRI remains the benchmark for the brain-wide mapping of neural circuits, fUSI has recently achieved whole-brain recordings at a similar spatial-temporal resolution (Brunner et al., 2020; Rabut et al., 2019). While such volumetric measurements make fUSI an interesting candidate for complementary circuit recordings, whole-brain imaging is still in a stage of infancy compared to fMRI and is not widely available. Thus, some key features of fMRI, such as brain-wide connectivity analyses are not yet ideally suited for fUSI and have been mostly limited to a single slice field-of-view (Ferrier et al., 2020; Osmanski et al., 2014; Rabut et al., 2020). Also contrary to fMRI, in some scenarios, such as experiments involving adult rats (Macé et al., 2011; Sieu et al., 2015; Urban et al., 2015), fUSI requires the installation of a cranial window, which can impact the structure and function of the brain. However, this procedure is not always needed, as has been successfully demonstrated by transcranial fUSI

in young rats (Mairesse et al., 2019; Rideau et al., 2016) and mice (Deffieux et al., 2021; Tiran et al., 2017).

Despite the invasiveness of fUSI, it has the potential to extend the scope of brain-wide optogenetic-based circuit mapping by utilizing a portable device that facilitates recording in behaving animals (Dizeux et al., 2019; Sieu et al., 2015; Tiran et al., 2017; Urban et al., 2015). Nevertheless, only two studies to date have investigated the combination of circuit-based optogenetics and fUSI, whereby the activation of different cell populations in the superior colliculus of mice revealed different brain-wide responses that were linked to defensive behaviors (Brunner et al., 2020; Sans-Dublanc et al., 2021). This innovative work, along with the variety of fUSI studies examining brain activity during different functional states (Bergel et al., 2020, 2018), foreshadow the impending investigation of neural circuits underlying complex or even freely moving behaviors. Nevertheless, as an initial step towards this goal and to ensure proper interpretation of such work, the fUSI signal must first be validated alongside well-established and comparable imaging modalities such as fMRI.

To address this need in the current work, we investigated and characterized the sensitivity of both the fUSI and fMRI response to optogenetic stimulations applied to the primary motor circuit of mice. In particular, optogenetic manipulations are attractive for such an investigation (compared to sensory stimulation) because direct neuronal activation creates highly reproducible stimulation conditions. To obtain ground-truth evidence of neuronal activation and to cross-validate the different hemodynamic signals at these stimulus intensities, we also acquired local field potential recordings across the motor circuit in response to the same optogenetic stimulations. Overall, our results indicate that fUSI is more sensitive than fMRI for detecting optogenetically-induced neural activity and elicits activations patterns that better co-localize with neuronal activity.

## 2. Materials and Methods

### 2.1 Animals

Seven healthy Thy1-ChR2-YFP mice (4 male, 8–12 weeks old at implantation; The Jackson Laboratory, Bar Harbor, ME, stock no. 007612) were used for all experiments. Animals were not used for any previous procedures. Animals were housed in groups prior to surgery and individually after surgery in a 12-hour light-dark cycle. Animals were provided with food and water *ad libitum*; Uniprim antibiotic feed containing 67 mg Trimethoprim and 333 mg Sulfadiazine per gram was provided to the animals starting one week before and up until two weeks after cranial window surgery. Animal husbandry and experimental procedures were performed according to the guidelines of the National Institutes of Health and Stanford University Institutional Animal Care and Use Committee (IACUC).

### 2.2 Fiber Implantation

Mice were anesthetized with 3–4 % isoflurane in 100 % oxygen and fixed in a stereotactic frame. The subcutaneous administration of slow-release buprenorphine (0.5 mg/kg) was then provided to alleviate post-surgical discomfort. After shaving the head of the animal, it was cleaned by means of a triple scrub, alternating the application of 70% ethanol and Betadine.

Body temperature was maintained at 37 °C using a thermoresistive heating pad (PHC Inc., Bowdoin, ME, USA). Petrolatum ophthalmic ointment was applied to the eyes to prevent dryness. 250 μL of 0.5 % bupivacaine was injected under the scalp followed by a midline scalp incision. A small craniotomy was made in the skull and a custom-made 200 μm diameter fiber-optic implant was inserted into the primary motor cortex (+1.5 mm ML +0.86 mm AP −0.65 mm DV) at an angle of 30° from the horizontal. The implant was secured to the skull with Clearfil AP-X light-cured dental cement (Kuraray Noritake Dental Inc, Tokyo, Japan, stock no. 1721-KA). The skin was approximated around the implant and sutured. The animals recovered for at least three days before imaging.

### 2.3 Cranial Window Surgery

Animals were initially administered an intraperitoneal bolus of a ketamine-xylazine cocktail (80 mg/kg ketamine hydrochloride, Vedco Inc., St. Joseph, MO, USA; 5 mg/kg xylazine, Akorn Inc, Lake Forest, IL, USA) with additional injections given as needed to maintain surgical depth. At this point, animal preparation was identical to that described previously in the Fiber Implantation section, where applicable. A 5 mm AP × 8 mm ML cranial window was then cut into the skull using a dental drill; sterile saline was periodically applied to the skull to prevent overheating. The skull was then removed, and the dura was left intact. A 3D printed custom head mount was secured to the remaining skull surface with dental cement approximately 1 mm above the brain. The head mount cavity was filled with 2 % agarose and covered with a 50 μm thick polymethylpentene (PMP) film. A locking frame was attached to the inner ridge of the head mount to secure the PMP film and seal the window. A protector plate was then placed on top of the window and secured to the head mount with plastic screws. The animals recovered for up to one week before imaging.

#### 2.4.1 Functional Ultrasound Imaging Data Acquisition

Functional ultrasound imaging data was acquired with a Vantage 128 (Verasonics Inc, Kirkland, WA, USA) using a custom-made 128-channel linear ultrasound array with a central frequency of 15 MHz and pitch of 0.1 mm (Vermon, Tours, France). This probe provided a 100 × 100 μm in-plane resolution. Animals were initially anesthetized with 3–4 % isoflurane (Sigma-Aldrich, St. Louis, MO, USA) in 100 % $O_2$ and secured in a stereotaxic frame. At the beginning of each imaging session, the anesthetic mixture was then switched to 1.5% isoflurane in a combination of 20 % $O_2$ and 80 % medical air. The protector plate was then removed and the cranial window was washed with sterile saline solution. A thin layer of sterile ultrasound gel (Medline Industries, Inc., Northfield, IL, USA) was then applied between the cranial window and the linear ultrasound array, which was adjusted to fully encompass the boundaries of the brain. A high-resolution anatomical power Doppler image (PDI) was then collected in the coronal plane at bregma + 0 mm.

PDI acquisition is based on the concept of plane wave compounding. Accordingly, every 2 ms the brain was insonified with multiple plane waves and the backscattered echoes were coherently summed to form a single compound ultrasound image (CUI). Anatomical CUIs were created using plane wave emissions at 15 tilt angles (±12, ±10, ±8, ±6, ±4, ±2, 0°), and 200 CUIs were acquired at 500 Hz for a total acquisition time of 400 ms per PDI. Time-resolved PDI data were collected in the same way but utilized 9 tilt angles (±8, ±6,

±4, ±2, 0°) and 100 CUIs (500 Hz frame rate, 200 ms acquisition). A total of 240 CUI stacks were acquired every 1500 ms (for a run time of 6 min) and saved to a file on the host computer for subsequent analysis. The field of view was constrained to the brain; an apodization scheme was utilized to blind specific array elements that would transmit/receive signals outside of the brain, resulting in an image size of 160 × 220 voxels for anatomical data and of 80 × 110 voxels for functional data.

### 2.4.2 Functional Ultrasound Imaging Data Preprocessing

Functional ultrasound data pre-processing was performed in MATLAB (MathWorks, Inc., Natick, MA, USA) using custom scripts. Anatomical and functional CUI stacks from each frame were subjected to singular value decomposition where the first 20 singular vectors pertaining to static tissue components were removed and the remaining singular vectors were used to reconstruct the vascular signal (Demené et al., 2015). This reconstructed CUI stack was then high-pass filtered at 30 Hz with a $5^{th}$ order butterworth filter. Finally, the individual CUIs were squared and averaged across the image stack to form a single PDI. In particular, this clutter filter technique removed low-frequency information associated with cardiac pulsatility and tissue motion. This process was performed for the anatomical acquisition and at each time point within the time-resolved functional data. Functional data were smoothed with a 300 μm median filter for the sensitivity analysis. Unsmoothed data were utilized to analyze characteristics of venous and arterial signal components. The first 10 brain volumes were removed from each data set before further analysis.

### 2.5.1 Functional Magnetic Resonance Imaging Data Acquisition

Functional magnetic resonance imaging (fMRI) data was acquired with a Bruker BioSpec 70/30 USR small animal MR system (Bruker BioSpin MRI, Ettlingen, Germany) operating at 300MHz (7T). Animals were initially anesthetized with 3–4% isoflurane (Sigma-Aldrich, St. Louis, MO, USA) in 100% O2 and secured in a MRI-compatible cradle. At the beginning of each imaging session, the anesthetic mixture was then switched to 1.5% isoflurane in a combination of 20 % $O_2$ and 80 % medical air. The MR system was equipped with an 86 mm volume resonator (Bruker, Ettlingen, Germany) for transmission and a single-loop surface coil for signal reception. Global $1^{st}$ order shimming was followed by fieldmap-based local shimming (MAPSHIM) to maximize the homogeneity of the static $B_0$ magnetic field. fMRI data were acquired using a Gradient Echo Planar Imaging sequence (GE-EPI) with the following parameters: field-of-view (FOV) = 24 × 10.5 $mm^2$ and matrix size = 80 × 30 yielding an in-plane voxel dimension of 300 μm × 300 μm, echo time/repetition time (TE/TR) = 12/1500 ms, number of averages (NA) = 1, flip angle (FA) $\alpha$ = 60°, number of slices = 24, slice thickness = 500 μm, number of repetitions = 240, for a total acquisition time of 6 minutes.

T2-weighted anatomical reference images were acquired using a Rapid Acquisition with Rapid Enhancement (RARE) sequence with the following parameters: TE = 33 ms, TR = 2671 ms, RARE factor = 8.24, axial slices of 500 μm thickness with a FOV = 24 × 10.5 mm, and a matrix of 256 × 256. These images produced a nominal resolution of 93 × 41μm. The acquisition time was 5 min 42 sec.

#### 2.5.2 Functional Magnetic Resonance Imaging Data Processing

Functional MRI data pre-processing was performed in Matlab using the SPM12 toolbox and custom scripts. The first 10 brain volumes were removed from each dataset, and the remaining volumes were subjected to slice-timing correction, realignment to the first volume, and smoothing with a 1 × 1 × 1 voxel (FWHM, 300 um) Gaussian kernel.

### 2.6 Optimal fMRI and fUSI in the same subjects

To fairly compare fMRI and fUSI, we ensured that experimental conditions were optimal for each imaging modality. For fMRI, the implanted optic fiber protruded from the skull and accommodated a loop surface receive coil. In general, with only a fiber implanted, a 1 cm loop coil rested flush with scalp of the animal with minimal air gaps. After the cranial window was installed, a 2 cm coil was required due to the increased height and diameter of material extending upward from the skull. We computed the signal-to-noise (SNR) and temporal-SNR (tSNR) for both setups to determine the optimal fMRI setup. The 1 cm coil setup produced higher SNR and tSNR values (cortical region-of-interest) compared to the 2 cm coil setup. Therefore, for fMRI, we used the 1 cm coil before cranial window installation to compare with fUSI and the 2 cm coil after cranial window installation to ensure the integrity of brain function after skull removal. Only one standard fUSI experimental setup was available for the imaging parameters and orientation utilized in the current study.

#### 2.7.1 Electrophysiological Data Acquisition

Electrophysiological recordings were acquired at a sampling rate of 40 kHz with a Plexon OmniPlex Neural Recording Data Acquisition System (Plexon Inc., Dallas, TX, USA) and the PlexControl software. Animals were initially anesthetized with 3–4 % isoflurane (Sigma-Aldrich, St. Louis, MO, USA) in 100 % $O_2$ and secured in a stereotaxic frame. At the beginning of each recording session, the anesthetic mixture was then switched to 1.5% isoflurane in a combination of 20 % $O_2$ and 80 % medical air. The cranial window head mount was then removed. Bregma was identified from markings made on the head mount during installation and from vascular landmarks on the exposed brain. Two 16-channel linear electrode arrays (A1×16-5mm-50-703-A16 electrode array) (NeuroNexus Technologies, Ann Arbor, MI, USA) were then inserted into the bilateral primary motor cortex and striatum.

#### 2.7.2 Electrophysiological Data Processing

Local field potential (LFP) processing was performed in MATLAB using custom scripts. LFP traces were downsampled to 1 kHz and bandpass filtered between 8 and 12 Hz using a $5^{th}$ order Butterworth filter. This frequency band was chosen to specifically examine the brain-wide neuronal activity, if present, that was driven by the exogenous optogenetic stimulation (10 Hz, see section 2.8). Filtered LFP traces were then averaged across stimulation blocks and electrodes within a single animal for each stimulation intensity. Individual trials for all electrodes were visually inspected for transient artifacts which, if detected, were subsequently removed.

### 2.8 Optogenetic Stimulation

Prior to both fUSI and fMRI data collection, a 200 μm diameter optical fiber was connected to a 473 nm laser source (LaserGlow Technologies, Toronto, Canada) and coupled to the fiber-optic implant. For electrophysiological recordings, the removal of the head mount also removed the original optic fiber. Therefore, an optical fiber was coupled to the electrode inserted in the original stimulation site. Once the animal was secured in the stereotaxic frame (fUSI and electrophysiology) or the animal cradle (fMRI), an initial bolus of 0.1 mg/kg of dexmedetomidine was administered subcutaneously and the isoflurane level was reduced to 0.25%. Throughout a functional imaging/recording session, dexmedetomidine was also continuously infused subcutaneously at 0.2 mg/kg/hr. Body temperature was maintained at 37 °C using a thermoresistive heating pad (PHC Inc., Bowdoin, ME, USA) for fUSI and electrophysiological recordings or using a heating fan for fMRI. For fUSI and fMRI, breathing rate was continuously monitored using a MR-compatible Monitoring and Gating System for Small Animals (Model 1030, Small Animal Instruments, Inc., Stony Brook, NY, USA). The breathing rate was within the normal physiological range of 80 – 120 breath/min for all recordings.

At the beginning of each session, optical power was calibrated to 0.1, 0.5 or 1.0 mW at the implanted fiber's tip for different imaging scans/electrophysiology recordings. A single scan consisted of a block design with 60 s of baseline measurement followed by five (fUSI and fMRI) or 10 (electrophysiology) 12 s pulse trains (10 Hz, 20 ms pulse width) of light delivered every 60 s. This long stimulation period was used to ensure that the relatively slow hemodynamic response could be sufficiently sampled using both fUSI and fMRI under the current experimental conditions (0.67 Hz sample rate, see sections 2.4.1 and 2.5.1). This protocol was also chosen based on similar fMRI-based block stimulation paradigms previously used in our lab (Lee et al., 2016; Weitz et al., 2019) and others (Chan et al., 2017; Schmid et al., 2017). The MRI scanner was synchronized with the laser using a Master 8 stimulator (A.M.P.I., Jerusalem, Israel) and the ultrasound controller and electrophysiology recording system with dual function generators (Keysight Technologies, Santa Rosa, CA, USA). 1–2 scans/recordings were collected at each optical power in pseudo-random order for each modality.

### 2.9 Activation Maps and Time Series Analysis

Fixed effect analyses were performed at the animal and group level using a general linear model. Functional data was registered to an average anatomical image using a simple affine transformation. The design matrix was constructed by convolving the block stimulus with fourth-order gamma functions. The contrasts used to compute the activation maps for fUSI and fMRI contained 1's for the $1^{st}$ and $2^{nd}$ order gamma functions, respectively, and 0's elsewhere. Active voxels at the animal and group level were identified as those exhibiting a t-score magnitude greater than 2.84 and 2.81, respectively, after correcting for false-discovery rate. These thresholds were determined based on identifying the t-score corresponding to $p < 0.005$ in a t-distribution with $n\text{-}2$ degrees of freedom, where $n$ represents the number of independent measurements. At the individual animal level $n$ is equal to 230 (see sections 2.4 – 2.5 for details on run length) and at the group level (n =

7 animals) equal to 1610. Active voxels are overlaid on top of representative anatomical images.

Regional analyses were performed at the individual animal level. Each fMRI (the slice containing bregma + 0 mm) and fUSI dataset was registered to the Paxinos Atlas and segmented into 18 regions-of-interest. Time series from each voxel within a region were averaged together and then bandpass filtered with a $5^{th}$ order Butterworth with cutoff frequencies of 0.005 and 0.1 Hz. Therefore, for each animal, stimulation intensity and region, two time series were calculated, one for fMRI and one for fUSI. Time series were then converted to percent modulation or z-scores relative to a 30 s pre-stimulation baseline. The time series from each region was then averaged across animals.

### 2.10 fUSI Blood Flow Analysis

As previously mentioned, a power Doppler (PD) image is constructed as the incoherent summation of a temporally filtered CUI stack. However, this time-resolved image stack is specifically collected at a frame rate that can also capture the Doppler shifts of red blood cells traveling through the vasculature. The upper limit of measurable Doppler shifts corresponds to the maximum detectable blood flow velocity. Therefore, prior to incoherent summation, blood flow direction and velocity can also be extracted.

Blood flow velocity is calculated according to Eq. 1, where $v_z$ is the axial blood velocity, $f_0$ is the pulsed central frequency of the acoustic wave, $c$ is the speed of sound in neural tissue (1540 m/s), and $f_D$ is the doppler shifted frequency of the moving red blood cells (Mace et al., 2013).

$$v_z = \frac{c * f_D}{2 * f_0} \quad \text{Eq. 1}$$

We used an ultrafast PD acquisition frame rate of 500 Hz. Therefore, according to Nyquist's theorem, the maximum resolvable Doppler frequency was 250 Hz. When insonifying neural tissue at 15 MHz, the PD signal in the current work contained information from blood moving at a speed of up to 12.83 mm/s. Importantly, optical and photoacoustic imaging modalities have shown that cerebral blood flow velocities are well within this range (Santisakultarm et al., 2012; Yao et al., 2015).

Blood flow direction was identified from the anatomical PD images from each animal by separating the positive and negative power spectra of the compound ultrasound image stack. Individual voxels were then classified as containing blood flowing towards or away from the transducer based on if the positive or negative power spectrum, respectively, was stronger. These binary maps were used to mask, for each animal, significantly active voxels for each flow direction. This procedure is equivalent to assigning each active voxel a binary direction using the power spectrum, as previously described. The corresponding time series for each flow component within a brain region were then subjected to the same analysis as previously described.

### 2.11 Histology

To confirm ChR2 expression in the Thy1 mouse model used, we anesthetized a representative animal with pentobarbital, followed by transcardial perfusion with 0.1M phosphate-buffered saline (PBS) and chilled 4% paraformaldehyde (PFA) in PBS. The brain was extracted and fixed in 4% PFA overnight at 4 °C, followed by submersion in 20% sucrose in PBS for 48 hours at 4 °C. 40 μm thick coronal brain sections were acquired using a Microm 550 cryostat (Thermo Fisher Scientific, Waltham, MA, USA). Free floating sections were washed three times with 0.1M PBS for ten minutes at room temperature and then exposed to 200 ng/ml of DAPI in PBS for 20 min at room temperature. Sections were washed once more with 0.1M PBS for ten minutes and then mounted on glass slides with Fluoromount-G (SouthernBiotech, Birmingham, AL, USA).

### 2.12 Statistical Analysis

Statistical analysis was performed using custom R and Matlab scripts. Exact values of N for all tests can be found in the text, figures, and figure legends. A one-way ANOVA with a main effect of stimulation intensity was used to compare the average t-scores at different stimulation intensities for fMRI and fUSI. Post-hoc analysis was performed with Tukey's HSD test. A Wilcoxon rank-sum test was used to compare the voxel-wise linear model outputs for fUSI and fMRI. A two-way ANOVA with main effects of stimulation intensity and vessel type or imaging modality was used to compare the area under the curve or z-score and active voxel count for the arterial and venous fUSI responses and the fUSI and fMRI evokes responses, respectively. For these analyses, the false discovery rate correction was applied to the main effect p-values to correct for multiple comparisons.

## 3. Results

### 3.1 Optogenetically-induced fUSI responses can be detected through chronic cranial windows

For direct neuronal control, we used optogenetics that enable on-demand modulation of neural activity using the light-sensitive transmembrane protein Channelrhodopsin-2 (ChR2) (Boyden et al., 2005; Lee et al., 2016, 2010). Thy1-ChR2 mice were chosen due to the robust and well-characterized endogenous expression of ChR2 in layer V cortical neurons (Wu et al., 2015) (Figure 1D). To combine optogenetics and fUSI, we installed a custom chronic cranial window and implanted an optical fiber in the primary motor cortex (M1) of Thy1-ChR2 mice (n = 7) (Figure 1A–C). This setup targeted the stimulation of the well-defined M1 circuit that contains known projections to both contralateral and subcortical motor regions (e.g. striatum), all of which can easily be seen in a single coronal brain slice acquired by fUSI (Anderson et al., 2010; Li et al., 2015). Circuit activation was confirmed by examining the sequential activation of such downstream motor regions using local field potential recordings (Figure S1A). The chronic cranial window was filled with 2 % agarose, sealed with an acoustically transparent film and, during imaging, covered with a thin layer of sterile ultrasound gel. This setup enabled the acquisition of 5 × 7 mm single plane PD images (Figure 1E). To validate fUSI against fMRI in the same animals, fMRI was performed after fiber implantation, and fUSI was performed after subsequent cranial window installation. At the end of the experiment, electrophysiological recordings were

acquired to verify neuronal activity (Figures 1F). This longitudinal experimental design was specifically chosen to reduce important sources of variability, such as fiber location and response to both stimulation and anesthesia, which can arise during cross-sectional studies with different animals. By doing so, we aimed to minimize factors that could potentially bias the comparison between fMRI and fUSI.

For both fUSI and fMRI, repeated optogenetic stimulation in lightly anesthetized mice (0.25 % isoflurane, 0.2 mg/kg/hr dexmedetomidine) produced robust evoked activity of the ipsilateral M1 that grew in magnitude with increasing stimulation intensity (Figure 1G). For fMRI, the spatial extent of activation was mostly constrained to the site of stimulation, which is consistent with previous results using the same transgenic line (Kahn et al., 2013, 2011). Only for the largest stimulation intensity did we also observe modulation in the contralateral M1 for fMRI. By contrast, for fUSI we observed evoked responses throughout the M1 circuit (bilateral M1 and striatum) (Figure 1G), consistent with Thy1-ChR2 axonal projections (Wu et al., 2015). Importantly, we also recorded fMRI in a subset (n = 5) of these animals after the initial fMRI, cranial window installation, and fUSI to ensure that stimulus-evoked brain function was preserved after skull removal (Figure 1F). The physical presence of the cranial window required fMRI to be performed under suboptimal and lower SNR conditions (see section 2.6 and Figure S1B–E), which resulted in noisier time series and sparser activation maps compared to the first fMRI time point (Figure S1G, Figure S2D). Despite these differences, the results revealed activity patterns similar to those observed before cranial window installation in that we again observed robust modulation near the site of stimulation and little evoked response in the contralateral M1 and bilateral striatum (Figure S1G).

### 3.2 fUSI detects optogenetically-evoked neural activity with high sensitivity

Examination of the recorded fUSI and fMRI time series revealed a markedly different shape of the evoked response for the two modalities. The fMRI response rose quickly and was followed by a characteristic undershoot that resembles the $2^{nd}$ order gamma function commonly observed in fMRI research (Buxton et al., 2004). On the contrary, while the fUSI response also rose quickly, it subsequently fell back to the baseline activity level, supporting the recently characterized $1^{st}$ order gamma-like response (Aydin et al., 2020). Therefore, the hemodynamic responses for fUSI and fMRI were modeled as $1^{st}$ and $2^{nd}$ order gamma functions, respectively, in a general linear model to quantify brain activity voxel-wise for each modality and stimulation intensity (Figures 2B **and** S2A). These activation maps were divided into 18 regions of interest (ROIs) according to the Paxinos histological brain atlas (Paxinos and Franklin, 2008) to examine how different brain regions reacted to varying stimulation intensities (Figures S2B). The regions investigated belong to the M1 circuit within the field-of-view and consist of bilateral motor, sensory, and cingulate cortices, as well as the striatum.

We found that the t-scores of many voxels covaried linearly with stimulation strength. Applying exogenous stimuli, such as tactile whisker stimulation, to rodents has been shown to elicit such a linear relationship with neural activation (Devor et al., 2003), however, this association can become asymptotically nonlinear at very high intensities (Cardoso et

al., 2012). Nevertheless, with the low light intensities used in this study (power: 0.1 – 1 mW, irradiance: 0.8 – 8 mW/mm$^2$), this nonlinear behavior was not observed. We fit additional linear regression models to the activation maps at the voxel level and found that across all cortical regions (16) examined, 48 % and 50 % of voxels were significantly correlated with stimulus intensity for fMRI and fUSI, respectively (Figure 2C–D). These values are reasonable considering only 59 % of fMRI and 60 % of fUSI cortical voxels were activated across all stimulation intensities. Despite a similar proportion of cortical voxels being linearly modulated for each modality, the absolute number of voxels was notably different and is likely due to the different within-plane spatial resolution of the fUSI (100 × 100 μm) and fMRI (300 × 300 μm) techniques employed in the current work (see Methods).

Linear models are valuable for examining the sensitivity to exogenous stimuli by describing two complementary properties: a modulation index (slope) and a minimum modeled activation value (Figure 2C). Specifically, the modulation index describes how the detection of neural activation changes in response to changes in stimulation intensity. Similarly, the minimum modeled activation describes the strength of neural activity elicited at the lower bound of stimulation intensities (power: 0.1 mW, irradiance: 0.8 mW/mm$^2$) in which linear modulation was observed. A higher sensitivity is therefore represented by both a larger modulation index and minimum modeled activation. When observing the voxel-wise modulation index (Figure 2E) and minimum modeled activation (Figure 2F) maps, it was evident that the values for both properties were generally larger for fUSI compared to fMRI throughout the field-of-view. To clearly examine the sensitivity of each modality, we plotted the modulation indexes against the minimum modeled activation values for all cortical voxels that exhibited a significant linear coupling with stimulation intensity (Figure 2G). While there was an overlap between the fMRI and fUSI distributions, both the average modulation index value and minimum modeled activation value (Wilcoxon rank-sum text, both $p < 0.001$) were significantly larger for fUSI compared to fMRI (Figure 2G), indicating an overall increase in sensitivity for detecting neural activity. For this analysis, we did not compare voxel sensitivity in the striatum as no fMRI voxels in this region were significantly modulated at all intensities.

We performed the same analysis at the region level using significantly modulated voxels and found an analogous overall effect regarding the higher sensitivity of fUSI compared to fMRI. The ipsilateral M1, being directly activated, exhibited a similar modulation index for both modalities (fUSI: 9.0, fMRI: 9.3) but displayed a larger minimum modeled activation for fUSI (5.7) compared to fMRI (2.6) (Figure S2E–G). However, for downstream circuit components, we found that the average regional modulation index was 1.6 times larger and that the average regional minimum modeled activation value was 1.4 times larger for fUSI compared to fMRI (Figure S2E–F). These results parallel previous human and animal fMRI studies that describe the increased sensitivity of the CBV signal compared to the BOLD signal for detecting evoked neural activity (Huber et al., 2017; Zhao et al., 2006).

In addition to the general linear model analysis, we also compared the amplitude of the evoked fUSI and fMRI time series responses. To account for the difference in modality-specific baselines, we transformed the time series into z-scores relative to the corresponding 30 seconds of pre-stimulation recordings. At the voxel level, we found that the average

evoked z-score also increased with stimulation strength across the bilateral M1 for both modalities but were generally larger for fUSI (Figure 3A). When examining these responses at the region level across stimulation intensities, we found that the average z-score was significantly larger for fUSI compared to fMRI in both the ipsilateral and contralateral M1 (two-way ANOVA, $p < 0.005$ both) (Figure 3B). These results were further supported when examining the evoked signals recorded from the ipsilateral striatum (two-way ANOVA; ipsilateral $p < 0.005$, contralateral $p > 0.05$) (Figure S3A). The magnitude of the z-scores during stimulation in a noise ROI outside of the brain show similarly low noise values for both modalities (Figure S3B), suggesting that the larger fUSI z-scores represent enhanced signal detection.

Finally, to verify that the observed vascular measurements represent the underlying neuronal activity, we acquired local field potential (LFP) recordings from the bilateral M1 (Figure 3C) and striatum (Figure S3C) of the same mice in which we recorded fMRI and fUSI ($n = 4$). As expected, we observed a growing % baseline change of the LFP in the ipsilateral and contralateral M1 (Figure 3D) and striatum (Figure S3D) with increasing stimulation intensity. Specifically, we observed activation across the M1 circuit for both electrophysiological and fUSI recordings, indicating a strong co-localization of these signals. In general, these results show that the fUSI response was larger in amplitude than that of fMRI and better reflected neuronal activation, further supporting the increased sensitivity of the fUSI signal.

We confirmed that all these signals were generated in response to optogenetically-induced neuronal activity by acquiring fMRI, fUSI and electrophysiological recordings in non-ChR2 expressing animals ($n = 2$). We found no evoked response in these animals for any of the three techniques in response to low intensity optogenetic stimulations (power ≤ 1 mW, irradiance ≤ 8 mW/mm$^2$) (Figure S3E–F). This indicates that the optogenetic protocol used in the current work did not cause heating-induced artifacts or unexpected neurophysiological responses that have previously been described for both fMRI and fUSI at higher stimulation intensities (power ≥ 2 mW, irradiance ≥ 18 mW/mm$^2$) (Albers et al., 2019; Christie et al., 2013; Rungta et al., 2017; Schmid et al., 2017).

### 3.3 Functional ultrasound imaging reveals vessel-specific hemodynamic responses to optogenetic stimulation

To examine the specificity of the fUSI signal, we decomposed the hemodynamic response into arterial and venous components by identifying the blood flow direction of individual vessels. Imaging the functional response of individual vessels and vessel types can also be performed using fMRI and photoacoustic techniques, however, such exemplary approaches offer notably less portability and spatial coverage of the circuit of interest (Yao et al., 2015; Yu et al., 2016). Functional ultrasound imaging can detect the axial movement (to or from the transducer) of red blood cells in the vasculature by examining the PD power spectrum of individual brain voxels (Figures 4A) (Macé et al., 2011). This blood flow information and the well documented neurovascular architecture can aid in identifying arterial and venous vessel networks throughout the brain. Specifically, blood vessels that perpendicularly penetrate the cortex are the primary pathways for perfusion between the pial vessels running

along the dorsal surface of the brain and subcortical vascular networks (Blinder et al., 2013; Shih et al., 2015). At the individual vessel scale, optical imaging techniques have consistently shown that descending arterioles and ascending venules in the mouse cortex carry blood away from and towards the brain surface, respectively (Baran et al., 2015).

By expanding this finding to the field-of-view offered by fUSI, we used the voxel-wise flow direction and vessel orientation throughout the cortex to identify significantly activated arterial and venous voxels (Figure 4B–C). When examining the activation dynamics across cortical regions, we observed a significant increase in the area under the curve (AUC) of the evoked response for arterioles compared to venules in the ipsilateral and contralateral M1 (two-way ANOVA, $p < 0.05$ both) (Figure 4D–E). Interestingly, the difference between the arterial and venous AUC was detected despite similar numbers of arterial and venous voxels being activated (Figure 4F–G), excluding the potentially confounding effects of a vessel-type activation bias. We observed strikingly similar results in the striatum (two-way ANOVA; ipsilateral $p < 0.01$, contralateral $p < 0.005$) (Figure S4), however, the relationship between axial blood flow direction and vessel type in subcortical structures has yet to be fully defined due to high vessel tortuosity in deeper brain regions. Nevertheless, these results show that fUSI can identify distinct dynamic features of vascular subunits within neural circuits, which may in the future help better understand the processes underlying neurovascular coupling.

## 4. Discussion

Functional ultrasound imaging is a tool that has recently emerged as a strong complement to other popular neuroimaging modalities such as fMRI (Boido et al., 2019) and two-photon imaging (Aydin et al., 2020; Boido et al., 2019; Rungta et al., 2017). These techniques exhibit distinct advantages that include spatial coverage and non-invasiveness (fMRI), portability (fUSI), and spatial resolution (two-photon) that, when combined, can facilitate the investigation of key scientific questions involving the brain-wide neurovascular responses. Functional MRI has been the standard for characterizing brain-wide neural circuits in animals due to the distinct ability to measure whole-brain dynamics driven by the activity of individual cell types. Nevertheless, we show in the current work that fUSI can detect optogenetically-induced neural activity with higher sensitivity than fMRI. Overall, when neural activation (t-scores) was modeled as a linear function of stimulation intensity, we found that fUSI exhibited not only a larger minimum modeled activation than fMRI, but also a larger modulation index in response to adjustments in stimulus intensity (Figure 2, S2). This heightened sensitivity was further supported by a significant increase in the magnitude of the evoked circuit-wide response (z-scores) of fUSI compared to that of fMRI (Figure 3, S3).

These results fall in line with a recent study that also investigated the fUSI and BOLD fMRI response (Boido et al., 2019). In Boido et al., low-intensity olfactory stimulation induced widespread activation of the olfactory bulb for fUSI, but only sparse activation for fMRI. Interestingly, this effect was observed when using a very high field strength (17.2T) and supports our data that was collected at a lower, albeit more common field strength (7T). While optogenetic stimulations are able to directly and consistently elicit neuronal activity,

light intensity cannot be increased as easily as olfactory stimulation due to potential imaging and/or physiological confounds (Albers et al., 2019; Christie et al., 2013; Rungta et al., 2017; Schmid et al., 2017). Therefore, in the current work we used only low intensity optogenetic stimulations that are below thresholds known to cause thermal complications, and confirmed the lack of such activity in naïve animals (Figure S2E–F). Overall, the use of both optogenetic and olfactory stimulations suggest that fUSI is a more sensitive reporter of neural activity than fMRI, however, the different intensity limits of these stimulus types indicate that experimental settings must be considered when choosing which imaging modality to use. This is particularly true for anesthetized experiments without implanted optic fibers, as more advanced fMRI equipment such as CryoProbes can increase the SNR and quality of fMRI data but offer restricted space above the head (Schlegel et al., 2018).

The investigation of neurovascular coupling is a particularly interesting application for combining micro- and mesoscale signals associated with various imaging modalities, including fUSI. Along these lines, while detailed investigations have characterized the relationship between spiking, synaptic, and LFP activity with the BOLD fMRI signal (Magri et al., 2012; Viswanathan and Freeman, 2007), such associations are only starting to emerge for fUSI. For example, simultaneous micro- and mesoscale recordings have recently linked calcium levels and RBC velocities recorded from individual neurons and vessels, respectively, with the CBV response recorded from individual fUSI voxels (Aydin et al., 2020). Other work examining simultaneous or sequential fUSI and electrical recordings have also established a direct relationship between these two signals (Boido et al., 2019; Nunez-Elizalde et al., 2021). While the current work did not specifically examine such a relationship, we observed electrophysiological activity across all stimulation intensities that strongly co-localized with the activity patterns of fUSI (Figure 3). We also found that different vessel types exhibit distinct vascular responses to evoked neuronal activity in a circuit-dependent manner (Figure 4), suggesting that universal brain-wide transformations may not fully explain the mesoscale representation of local neuronal activity. In fact, two-photon studies have shown that the hemodynamic response is mostly influenced by arterial vasodynamics, which highlight the importance of examining neurovascular coupling in the context of arterial and venous components separately (Devor et al., 2008, 2007). Therefore, complementary fUSI-based approaches involving direct neuronal activation via optogenetics, as was performed in the current work, as well as super-resolution vascular microscopy (Errico et al., 2015) may help expand this research area in the future to the investigation of global neural responses with vessel-type specificity.

Furthermore, the different hemodynamic response shapes observed between fUSI and BOLD fMRI (Figure 2A) indicate that different hemodynamic readouts may be useful for identifying various neurovascular mechanisms. Specifically, the fUSI signal (and the CBV-based fMRI signal) is most sensitive to the influx and subsequent dissipation of localized blood volume recruited due to the metabolic demands of neuronal activation (Figure 1G) (Mace et al., 2013). By contrast, the BOLD fMRI signal is most sensitive to the deoxygenated hemoglobin (Hbr) content within this blood volume. As neuronal firing consumes oxygen, the Hbr level within the blood increases and is considered the main contributor to the BOLD undershoot (Figure 1G) (Buxton et al., 2004). This disparity further highlights the need for multimodal approaches that bridge neuronal and vascular signals to

map the micro- and meso-representations of brain activity (Chen et al., 2019; Schulz et al., 2012).

Portability is a principal characteristic of fUSI that is becoming increasingly utilized for investigating brain functions in behaving rodents (Brunner et al., 2021, 2020; Macé et al., 2018; Urban et al., 2015). Here, in a head-fixed and anesthetized context, we quantified and cross-validated the ability of fUSI to image large-scale activity patterns elicited by the manipulation of specific neuronal populations. This work may in the future extend to the context of behaving or freely moving optogenetic studies as the footprint and weight of ultrasound probe technology becomes smaller and more easily paired with head fixation or tethering setups. Thus, this study contributes to a framework whereby combining fUSI and optogenetics can help answer systems neuroscience questions by linking brain-wide networks to corresponding behavioral readouts (Brunner et al., 2020; Edelman and Macé, 2021; Sans-Dublanc et al., 2021).

Transcranial fUSI in rodents has recently gained significant popularity (Deffieux et al., 2021; Mairesse et al., 2019; Rideau et al., 2016; Tiran et al., 2017), establishing this approach alongside similar noninvasive imaging modalities such as fMRI (Duffy et al., 2020; Lee et al., 2016, 2010; Liu et al., 2015; Weitz et al., 2019, 2015) and photoacoustic imaging (Yao et al., 2015). Nevertheless, in the current work, we chose to utilize a chronic cranial window for fUSI to eliminate the risk of ultrasound attenuation through the skull and to ensure that high-quality signals were acquired across the same field-of-view in which we acquired fMRI. It is therefore important to note that various works have reported minimal damage caused by similar skull manipulations (Ghanbari et al., 2019; Urban et al., 2014). Nevertheless, others have found that such a procedure can lead to dysfunctions of natural vasomotor oscillations and the excitation-inhibition balance of the brain (Drew et al., 2010; Kato et al., 2017). To determine if skull removal significantly affected the optogenetically-induced neural activity detected in the current work, we acquired fMRI data at a second time point, after cranial window installation and fUSI. This post-cranial window fMRI exhibited lower SNR due to the physical constraints associated with accommodating both an MR loop receive coil and the implant (see Section 2.6 and Figure S1B–F for details). The lower SNR manifested as higher fluctuations in the observed time series compared to the pre-cranial window fMRI (Figure S1G), which further translated to sparser and weaker activation maps (Figure S2D). Nevertheless, we still observed similar overall activation patterns for both fMRI time points in the sense that optogenetic modulation was mainly observed near the site of stimulation. Thus, the post-cranial window fMRI was considered suboptimal and was used merely to verify intact stimulus-evoked brain activity whereas the pre-cranial window fMRI was performed under optimal conditions and used to compare with fUSI.

## 5. Conclusion

Overall, fUSI continues to be a promising approach to brain-wide functional imaging that can complement an array of other micro- and mesoscale imaging modalities. In the current work, we found that fUSI is a more sensitive hemodynamic readout of optogenetically-induced neuronal activity compared to fMRI. By isolating the arterial and venous components of the vascular response, we also found that fUSI can map large-scale

neural circuit activity with vessel-type specificity. Techniques such as the fUSI approach demonstrated in the current work, in addition to the inherent portability of fUSI systems, may in the future facilitate neural-circuit analysis underlying behavior at an unprecedented scale and coverage.

## Supplementary Material

Refer to Web version on PubMed Central for supplementary material.

## Acknowledgements

This work was supported by NIH/NIMH RF1MH114227 and NIH/NINDS DP1NS116783. The authors thank the entire Lee lab and Dr. Michael Lin for the helpful comments.

## Data and Code Availability

Requests for raw data should be directed to and will be fulfilled by the Lead Contact, Jin Hyung Lee (ljinhy@stanford.edu), Stanford University.

## References

Albers F, Wachsmuth L, Schache D, Lambers H, Faber C, 2019. Functional MRI Readouts From BOLD and Diffusion Measurements Differentially Respond to Optogenetic Activation and Tissue Heating. Front. Neurosci 13. 10.3389/fnins.2019.01104

Anderson CT, Sheets PL, Kiritani T, Shepherd GMG, 2010. Sublayer-specific microcircuits of corticospinal and corticostriatal neurons in motor cortex. Nat. Neurosci 13, 739–744. 10.1038/nn.2538 [PubMed: 20436481]

Aydin A-K, Haselden WD, Goulam Houssen Y, Pouzat C, Rungta RL, Demené C, Tanter M, Drew PJ, Charpak S, Boido D, 2020. Transfer functions linking neural calcium to single voxel functional ultrasound signal. Nat. Commun 11, 2954. 10.1038/s41467-020-16774-9 [PubMed: 32528069]

Baran U, Li Y, Wang RK, 2015. Vasodynamics of pial and penetrating arterioles in relation to arteriolo-arteriolar anastomosis after focal stroke. Neurophotonics 2, 025006. 10.1117/1.NPh.2.2.025006 [PubMed: 26158010]

Bergel A, Deffieux T, Demené C, Tanter M, Cohen I, 2018. Local hippocampal fast gamma rhythms precede brain-wide hyperemic patterns during spontaneous rodent REM sleep. Nat. Commun 10.1038/s41467-018-07752-3

Bergel A, Tiran E, Deffieux T, Demené C, Tanter M, Cohen I, 2020. Adaptive modulation of brain hemodynamics across stereotyped running episodes. Nat. Commun 10.1038/s41467-020-19948-7

Bernal-Casas D, Lee HJ, Weitz AJ, Lee JH, 2017. Studying Brain Circuit Function with Dynamic Causal Modeling for Optogenetic fMRI. Neuron 93, 522–532.e5. 10.1016/j.neuron.2016.12.035 [PubMed: 28132829]

Blinder P, Tsai PS, Kaufhold JP, Knutsen PM, Suhl H, Kleinfeld D, 2013. The cortical angiome: an interconnected vascular network with noncolumnar patterns of blood flow. Nat. Publ. Gr 16. 10.1038/nn.3426

Boido D, Rungta RL, Osmanski B-F, Roche M, Tsurugizawa T, Le Bihan D, Ciobanu L, Charpak S, 2019. Mesoscopic and microscopic imaging of sensory responses in the same animal. Nat. Commun 10, 1110. 10.1038/s41467-019-09082-4 [PubMed: 30846689]

Boyden ES, Zhang F, Bamberg E, Nagel G, Deisseroth K, 2005. Millisecond-timescale, genetically targeted optical control of neural activity. Nat. Neurosci 8, 1263–1268. 10.1038/nn1525 [PubMed: 16116447]

Brunner C, Grillet M, Sans-Dublanc A, Farrow K, Lambert T, Macé E, Montaldo G, Urban A, 2020. A Platform for Brain-wide Volumetric Functional Ultrasound Imaging and Analysis of Circuit Dynamics in Awake Mice. Neuron 108, 1–15. 10.1016/j.neuron.2020.09.020 [PubMed: 33058761]

Brunner C, Grillet M, Urban A, Roska B, Montaldo G, Macé E, 2021. Whole-brain functional ultrasound imaging in awake head-fixed mice. Nat. Protoc 1–25. 10.1038/s41596-021-00548-8

Buxton RB, Uludağ K, Dubowitz DJ, Liu TT, 2004. Modeling the hemodynamic response to brain activation, in: NeuroImage. 10.1016/j.neuroimage.2004.07.013

Cardoso MMB, Sirotin YB, Lima B, Glushenkova E, Das A, 2012. The neuroimaging signal is a linear sum of neurally distinct stimulus-and task-related components. Nat. Neurosci 15, 1298–1306. 10.1038/nn.3170 [PubMed: 22842146]

Chan RW, Leong ATL, Ho LC, Gao PP, Wong EC, Dong CM, Wang X, He J, Chan Y-S, Lim LW, Wu EX, 2017. Low-frequency hippocampal–cortical activity drives brain-wide resting-state functional MRI connectivity. Proc. Natl. Acad. Sci 114, E6972–E6981. 10.1073/pnas.1703309114 [PubMed: 28760982]

Chen X, Sobczak F, Chen Y, Jiang Y, Qian C, Lu Z, Ayata C, Logothetis NK, Yu X, 2019. Mapping optogenetically-driven single-vessel fMRI with concurrent neuronal calcium recordings in the rat hippocampus. Nat. Commun 10, 5239. 10.1038/s41467-019-12850-x [PubMed: 31748553]

Christie IN, Wells JA, Southern P, Marina N, Kasparov S, Gourine AV, Lythgoe MF, 2013. fMRI response to blue light delivery in the naïve brain: Implications for combined optogenetic fMRI studies. Neuroimage 66, 634–641. 10.1016/j.neuroimage.2012.10.074 [PubMed: 23128081]

Deffieux T, Demené C, Tanter M, 2021. Functional Ultrasound Imaging: A New Imaging Modality for Neuroscience. Neuroscience. 10.1016/j.neuroscience.2021.03.005

Demené C, Deffieux T, Pernot M, Osmanski BF, Biran V, Gennisson JL, Sieu LA, Bergel A, Franqui S, Correas JM, Cohen I, Baud O, Tanter M, 2015. Spatiotemporal Clutter Filtering of Ultrafast Ultrasound Data Highly Increases Doppler and fUltrasound Sensitivity. IEEE Trans. Med. Imaging 34, 2271–2285. 10.1109/TMI.2015.2428634 [PubMed: 25955583]

Devor A, Dunn AK, Andermann ML, Ulbert I, Boas DA, Dale AM, 2003. Coupling of total hemoglobin concentration, oxygenation, and neural activity in rat somatosensory cortex. Neuron 39, 353–359. 10.1016/S0896-6273(03)00403-3 [PubMed: 12873390]

Devor A, Hillman EMC, Tian P, Waeber C, Teng IC, Ruvinskaya L, Shalinsky MH, Zhu H, Haslinger RH, Narayanan SN, Ulbert I, Dunn AK, Lo EH, Rosen BR, Dale AM, Kleinfeld D, Boas DA, 2008. Stimulus-Induced Changes in Blood Flow and 2-Deoxyglucose Uptake Dissociate in Ipsilateral Somatosensory Cortex. J. Neurosci 28, 14347–14357. 10.1523/JNEUROSCI.4307-08.2008 [PubMed: 19118167]

Devor A, Tian P, Nishimura N, Teng IC, Hillman EMC, Narayanan SN, Ulbert I, Boas DA, Kleinfeld D, Dale AM, 2007. Suppressed Neuronal Activity and Concurrent Arteriolar Vasoconstriction May Explain Negative Blood Oxygenation Level-Dependent Signal. J. Neurosci 27, 4452–4459. 10.1523/JNEUROSCI.0134-07.2007 [PubMed: 17442830]

Dizeux A, Gesnik M, Ahnine H, Blaize K, Arcizet F, Picaud S, Sahel JA, Deffieux T, Pouget P, Tanter M, 2019. Functional ultrasound imaging of the brain reveals propagation of task-related brain activity in behaving primates. Nat. Commun 10. 10.1038/s41467-019-09349-w

Drew PJ, Shih AY, Driscoll JD, Knutsen PM, Blinder P, Davalos D, Akassoglou K, Tsai PS, Kleinfeld D, 2010. Chronic optical access through a polished and reinforced thinned skull. Nat. Methods 7, 981–984. 10.1038/nmeth.1530 [PubMed: 20966916]

Duffy BA, Choy MK, Lee JH, 2020. Predicting Successful Generation and Inhibition of Seizure-like Afterdischarges and Mapping Their Seizure Networks Using fMRI. Cell Rep. 30, 2540–2554.e4. 10.1016/j.celrep.2020.01.095 [PubMed: 32101734]

Edelman BJ, Macé E, 2021. Functional ultrasound brain imaging: bridging networks, neurons and behavior. Curr. Opin. Biomed. Eng 100286. 10.1016/j.cobme.2021.100286

Errico C, Pierre J, Pezet S, Desailly Y, Lenkei Z, Couture O, Tanter M, 2015. Ultrafast ultrasound localization microscopy for deep super-resolution vascular imaging. Nature 527, 499–502. 10.1038/nature16066 [PubMed: 26607546]

Ferrier J, Tiran E, Deffieux T, Tanter M, Lenkei Z, 2020. Functional imaging evidence for task-induced deactivation and disconnection of a major default mode network hub in the mouse brain. Proc. Natl. Acad. Sci 201920475. 10.1073/pnas.1920475117

Ghanbari L, Carter RE, Rynes ML, Dominguez J, Chen G, Naik A, Hu J, Sagar MAK, Haltom L, Mossazghi N, Gray MM, West SL, Eliceiri KW, Ebner TJ, Kodandaramaiah SB, 2019.

Cortex-wide neural interfacing via transparent polymer skulls. Nat. Commun 10, 1500. 10.1038/s41467-019-09488-0 [PubMed: 30940809]

Huber L, Handwerker DA, Jangraw DC, Chen G, Hall A, Stüber C, Gonzalez-Castillo J, Ivanov D, Marrett S, Guidi M, Goense J, Poser BA, Bandettini PA, 2017. High-Resolution CBV-fMRI Allows Mapping of Laminar Activity and Connectivity of Cortical Input and Output in Human M1. Neuron 96, 1253–1263.e7. 10.1016/j.neuron.2017.11.005 [PubMed: 29224727]

Kahn I, Desai M, Knoblich U, Bernstein J, Henninger M, Graybiel AM, Boyden ES, Buckner RL, Moore CI, 2011. Characterization of the Functional MRI Response Temporal Linearity via Optical Control of Neocortical Pyramidal Neurons. J. Neurosci 31, 15086–15091. 10.1523/JNEUROSCI.0007-11.2011 [PubMed: 22016542]

Kahn I, Knoblich U, Desai M, Bernstein J, Graybiel AM, Boyden ES, Buckner RL, Moore CI, 2013. Optogenetic drive of neocortical pyramidal neurons generates fMRI signals that are correlated with spiking activity. Brain Res. 1511, 33–45. 10.1016/j.brainres.2013.03.011 [PubMed: 23523914]

Kato HK, Asinof SK, Isaacson JS, 2017. Network-Level Control of Frequency Tuning in Auditory Cortex. Neuron 95, 412–423.e4. 10.1016/j.neuron.2017.06.019 [PubMed: 28689982]

Lee HJ, Weitz AJ, Bernal-Casas D, Duffy BA, Choy MK, Kravitz AV, Kreitzer AC, Lee JH, 2016. Activation of Direct and Indirect Pathway Medium Spiny Neurons Drives Distinct Brain-wide Responses. Neuron 91, 412–424. 10.1016/j.neuron.2016.06.010 [PubMed: 27373834]

Lee JH, Durand R, Gradinaru V, Zhang F, Goshen I, Kim DS, Fenno LE, Ramakrishnan C, Deisseroth K, 2010. Global and local fMRI signals driven by neurons defined optogenetically by type and wiring. Nature 465, 788–792. 10.1038/nature09108 [PubMed: 20473285]

Li N, Chen T-W, Guo ZV, Gerfen CR, Svoboda K, 2015. A motor cortex circuit for motor planning and movement. Nature 519, 51–56. 10.1038/nature14178 [PubMed: 25731172]

Liu J, Lee HJ, Weitz AJ, Fang Z, Lin P, Choy M, Fisher R, Pinskiy V, Tolpygo A, Mitra P, Schiff N, Lee JH, 2015. Frequency-selective control of cortical and subcortical networks by central thalamus. Elife 4. 10.7554/elife.09215

Macé E, Montaldo G, Cohen I, Baulac M, Fink M, Tanter M, 2011. Functional ultrasound imaging of the brain. Nat. Methods 8, 662–664. 10.1038/nmeth.1641 [PubMed: 21725300]

Mace E, Montaldo G, Osmanski BF, Cohen I, Fink M, Tanter M, 2013. Functional ultrasound imaging of the brain: Theory and basic principles. IEEE Trans. Ultrason. Ferroelectr. Freq. Control 60, 492–506. 10.1109/TUFFC.2013.2592 [PubMed: 23475916]

Macé É, Montaldo G, Trenholm S, Cowan C, Brignall A, Urban A, Roska B, 2018. Whole-Brain Functional Ultrasound Imaging Reveals Brain Modules for Visuomotor Integration. Neuron 100, 1241–1251.e7. 10.1016/j.neuron.2018.11.031 [PubMed: 30521779]

Magri C, Schridde U, Murayama Y, Panzeri S, Logothetis NK, 2012. The Amplitude and Timing of the BOLD Signal Reflects the Relationship between Local Field Potential Power at Different Frequencies. 10.1523/JNEUROSCI.3985-11.2012

Mairesse J, Zinni M, Pansiot J, Hassan-Abdi R, Demene C, Colella M, Charriaut-Marlangue C, Rideau Batista Novais A, Tanter M, Maccari S, Gressens P, Vaiman D, Soussi-Yanicostas N, Baud O, 2019. Oxytocin receptor agonist reduces perinatal brain damage by targeting microglia. Glia 67, 345–359. 10.1002/glia.23546 [PubMed: 30506969]

Nunez-Elizalde AO, Krumin M, Reddy CB, Montaldo G, Urban A, Harris KD, Carandini M, 2021. Neural basis of functional ultrasound signals. bioRxiv 2021.03.31.437915. 10.1101/2021.03.31.437915

Osmanski B-F, Pezet S, Ricobaraza A, Lenkei Z, Tanter M, 2014. Functional ultrasound imaging of intrinsic connectivity in the living rat brain with high spatiotemporal resolution. Nat. Commun 5, 5023. 10.1038/ncomms6023

Paxinos G, Franklin K, 2008. The Mouse Brain in Stereotaxic Coordinates, Compact, The Mouse Brain in Stereotaxic Coordinates.

Rabut C, Correia M, Finel V, Pezet S, Pernot M, Deffieux T, Tanter M, 2019. 4D functional ultrasound imaging of whole-brain activity in rodents. Nat. Methods 16, 994–997. 10.1038/s41592-019-0572-y [PubMed: 31548704]

Rabut C, Ferrier J, Bertolo A, Osmanski B, Mousset X, Pezet S, Deffieux T, Lenkei Z, Tanter M, 2020. Pharmaco-fUS: Quantification of pharmacologically-induced dynamic changes in brain perfusion

and connectivity by functional ultrasound imaging in awake mice. Neuroimage 222, 117231. 10.1016/j.neuroimage.2020.117231 [PubMed: 32795659]

Rideau A, Novais B, Pham H, Van De Looij Y, Bernal M, Mairesse J, Zana-Taieb E, Colella M, Jarreau P-H, Pansiot J, Dumont F, Ephane Sizonenko S, Gressens P, Charriaut-Marlangue C, Tanter M, Demene C, Vaiman D, Baud O, 2016. Transcriptomic Regulations in Oligodendroglial and Microglial Cells Related to Brain Damage following Fetal Growth Restriction. 10.1002/glia.23079

Rubin JM, Bude RO, Carson PL, Bree RL, Adler RS, 1994. Power Doppler US: a potentially useful alternative to mean frequency-based color Doppler US. Radiology 190, 853–856. 10.1148/radiology.190.3.8115639 [PubMed: 8115639]

Rungta RL, Osmanski B-F, Boido D, Tanter M, Charpak S, 2017. Light controls cerebral blood flow in naive animals. Nat. Commun 8, 14191. 10.1038/ncomms14191 [PubMed: 28139643]

Sans-Dublanc A, Chrzanowska A, Reinhard K, Lemmon D, Nuttin B, Lambert T, Montaldo G, Urban A, Farrow K, 2021. Optogenetic fUSI for brain-wide mapping of neural activity mediating collicular-dependent behaviors. Neuron 109, 1888–1905.e10. 10.1016/j.neuron.2021.04.008 [PubMed: 33930307]

Santisakultarm TP, Cornelius NR, Nishimura N, Schafer AI, Silver RT, Doerschuk PC, Olbricht WL, Schaffer CB, 2012. In vivo two-photon excited fluorescence microscopy reveals cardiac- and respiration-dependent pulsatile blood flow in cortical blood vessels in mice. Am. J. Physiol. - Hear. Circ. Physiol 302. 10.1152/ajpheart.00417.2011

Schlegel F, Sych Y, Schroeter A, Stobart J, Weber B, Helmchen F, Rudin M, 2018. Fiber-optic implant for simultaneous fluorescence-based calcium recordings and BOLD fMRI in mice. Nat. Publ. Gr 13. 10.1038/nprot.2018.003

Schmid F, Wachsmuth L, Albers F, Schwalm M, Stroh A, Faber C, 2017. True and apparent optogenetic BOLD fMRI signals. Magn. Reson. Med 77, 126–136. 10.1002/mrm.26095 [PubMed: 26778283]

Schulz K, Sydekum E, Krueppel R, Engelbrecht CJ, Schlegel F, Schröter A, Rudin M, Helmchen F, 2012. Simultaneous BOLD fMRI and fiber-optic calcium recording in rat neocortex. Nat. Methods 9, 597–602. 10.1038/nmeth.2013 [PubMed: 22561989]

Shih AY, Rühlmann C, Blinder P, Devor A, Drew PJ, Friedman B, Knutsen PM, Lyden PD, Matéo C, Mellander L, Nishimura N, Schaffer CB, Tsai PS, Kleinfeld D, 2015. Robust and Fragile Aspects of Cortical Blood Flow in Relation to the Underlying Angioarchitecture. Microcirculation 22, 204–218. 10.1111/micc.12195 [PubMed: 25705966]

Sieu LA, Bergel A, Tiran E, Deffieux T, Pernot M, Gennisson JL, Tanter M, Cohen I, 2015. EEG and functional ultrasound imaging in mobile rats. Nat. Methods 12, 831–834. 10.1038/nmeth.3506 [PubMed: 26237228]

Tiran E, Ferrier J, Deffieux T, Gennisson J-LL, Pezet S, Lenkei Z, Tanter M, 2017. Transcranial Functional Ultrasound Imaging in Freely Moving Awake Mice and Anesthetized Young Rats without Contrast Agent. Ultrasound Med. Biol 43, 1679–1689. 10.1016/j.ultrasmedbio.2017.03.011 [PubMed: 28476311]

Urban A, Dussaux C, Martel G, Brunner C, Mace E, Montaldo G, 2015. Real-time imaging of brain activity in freely moving rats using functional ultrasound. Nat. Methods 12, 873–878. 10.1038/nmeth.3482 [PubMed: 26192084]

Urban A, Mace E, Brunner C, Heidmann M, Rossier J, Montaldo G, 2014. Chronic assessment of cerebral hemodynamics during rat forepaw electrical stimulation using functional ultrasound imaging. Neuroimage 101, 138–149. 10.1016/j.neuroimage.2014.06.063 [PubMed: 25008960]

Viswanathan A, Freeman RD, 2007. Neurometabolic coupling in cerebral cortex reflects synaptic more than spiking activity. 10.1038/nn1977

Weitz AJ, Fang Z, Lee HJ, Fisher RS, Smith WC, Choy MK, Liu J, Lin P, Rosenberg M, Lee JH, 2015. Optogenetic fMRI reveals distinct, frequency-dependent networks recruited by dorsal and intermediate hippocampus stimulations. Neuroimage 107, 229–241. 10.1016/j.neuroimage.2014.10.039 [PubMed: 25462689]

Weitz AJ, Lee HJ, Choy MK, Lee JH, 2019. Thalamic Input to Orbitofrontal Cortex Drives Brain-wide, Frequency-Dependent Inhibition Mediated by GABA and Zona Incerta. Neuron 104, 1153–1167.e4. 10.1016/j.neuron.2019.09.023 [PubMed: 31668484]

Wu Y-W, Kim J-I, Tawfik VL, Lalchandani RR, Scherrer G, Ding JB, 2015. Input- and Cell-Type-Specific Endocannabinoid-Dependent LTD in the Striatum. Cell Rep. 10, 75–87. 10.1016/j.celrep.2014.12.005 [PubMed: 25543142]

Yao J, Wang Lidai, Yang JM, Maslov KI, Wong TTW, Li L, Huang CH, Zou J, Wang Lihong V., 2015. High-speed label-free functional photoacoustic microscopy of mouse brain in action. Nat. Methods 12, 407–410. 10.1038/nmeth.3336 [PubMed: 25822799]

Yu X, He Y, Wang M, Merkle H, Dodd SJ, Silva AC, Koretsky AP, 2016. Sensory and optogenetically driven single-vessel fMRI. Nat. Methods 13, 337–340. 10.1038/nmeth.3765 [PubMed: 26855362]

Zhao F, Wang P, Hendrich K, Ugurbil K, Kim SG, 2006. Cortical layer-dependent BOLD and CBV responses measured by spin-echo and gradient-echo fMRI: Insights into hemodynamic regulation. Neuroimage 30, 1149–1160. 10.1016/j.neuroimage.2005.11.013 [PubMed: 16414284]

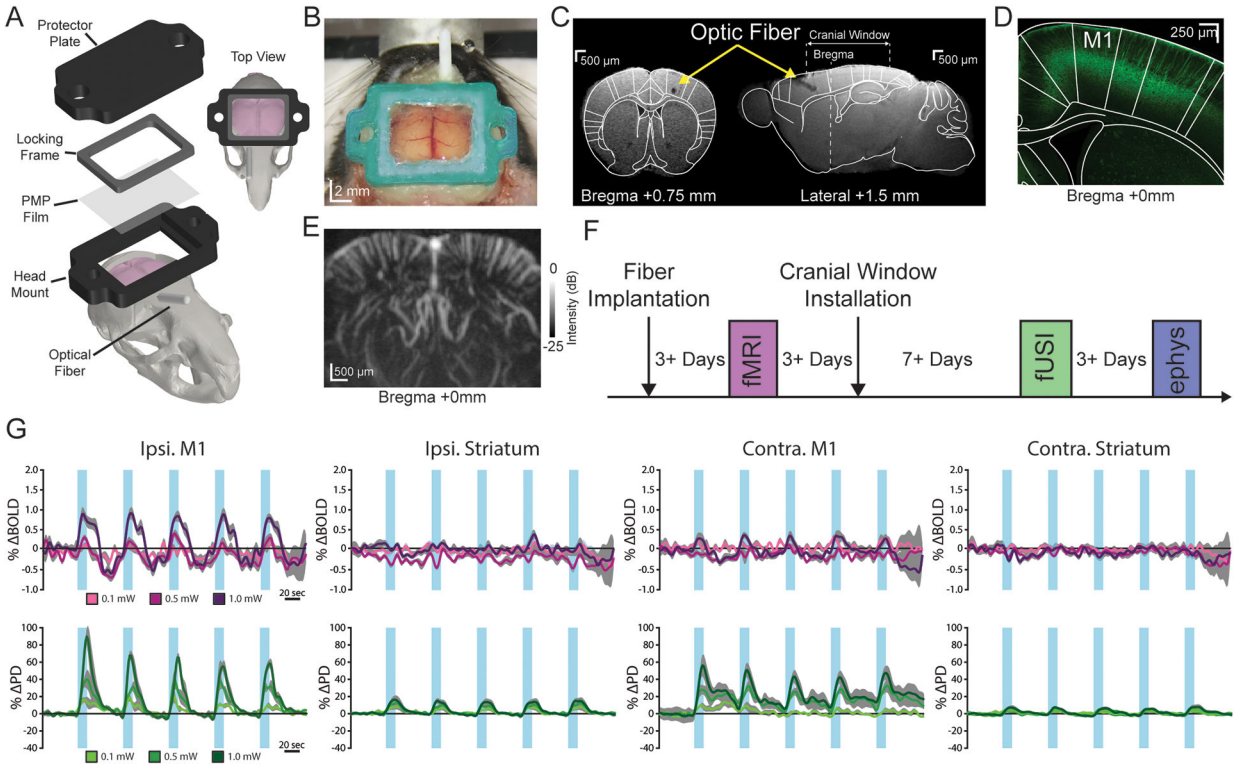


**Figure 1. Optogenetically-induced fUSI responses can be detected through chronic cranial windows.**

**(A)** Computer-aided design schematic of the cranial window and optic fiber installation. **(B)** Image of a chronic cranial window installed on a mouse. **(C)** Coronal (left) and sagittal (right) view of a structural magnetic resonance image (MRI) with a cranial window and optic fiber implanted in the right primary motor cortex (M1). **(D)** Representative histological image of endogenous ChR2-YFP expression in layer V of M1. **(E)** Power Doppler image depicting the coronal field of view at bregma +0 mm. **(F)** Experimental timeline for fUSI, fMRI, and electrophysiological recordings in response to optogenetic stimulations. **(G)** Average fMRI (pre-cranial window; top, purple) and fUSI (bottom, green) time series from the bilateral primary motor cortex (M1) and striatum during right M1 stimulation at 10 Hz. Data are presented as mean (color) ± SEM (shaded region). Increasing darkness of the lines represents increasing stimulation intensities. The blue vertical bars indicate stimulation periods.

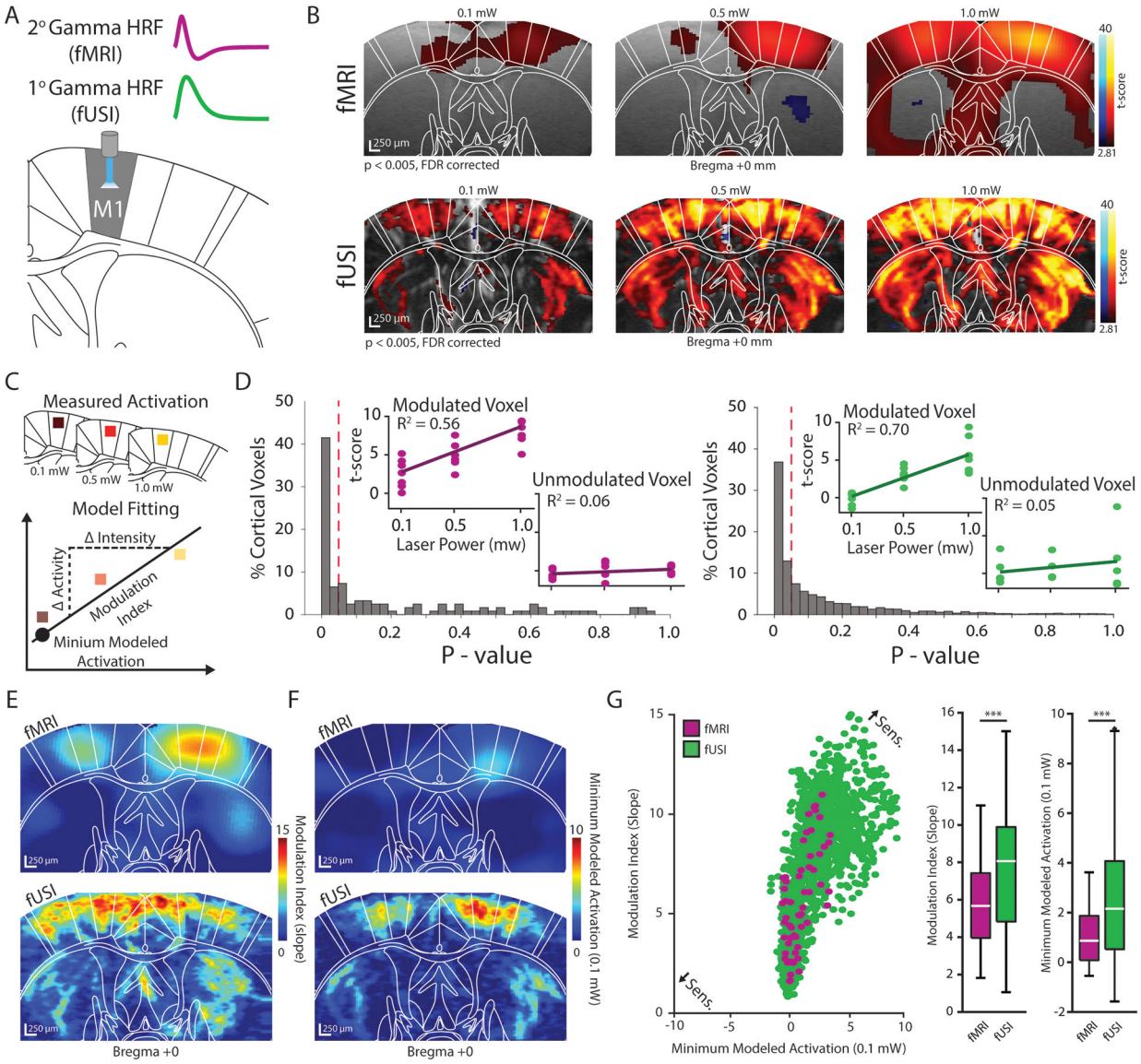


**Figure 2. Functional ultrasound imaging detects optogenetically-evoked neural activity with high sensitivity.**

**(A)** The evoked fMRI and fUSI responses clearly depict 2nd and 1st order gamma functions, respectively, and were used to model the activation dynamics voxel-wise throughout the field-of-view. **(B)** Group-level fMRI (top) and fUSI (bottom) activation maps for 0.1 mW (left), 0.5 mW (middle), 1.0 mW (right) stimulation were generated using a general linear model (n = 7 animals; $p < 0.005$, FDR corrected). Warm and cool colors indicate positive and negative t-scores, respectively. (**C**) Linear regression models were fit to the activation maps in (B) to determine a modulation index (slope) and minimum modeled activation (power: 0.1 mW, irradiance: 0.8 mW/mm$^2$) value for each voxel. (**D**) Normalized histograms of model p-values of all cortical voxels indicate that 48% and 50% of cortical voxels were linearly modulated by stimulation intensity for fMRI (left) and fUSI (right), respectively. Inlays show t-scores and models for example voxels that were significantly modulated and unmodulated. The red dotted line indicates the significance threshold of $p = 0.05$. **(E–F)**

Voxel-wise fMRI (top) and fUSI (bottom) modulation index (slope) (**E**) and minimum modeled activation (**F**) maps. (**G**) Sensitivity was evaluated for fMRI (purple) and fUSI (green) by plotting the minimum modeled activation values (x-axis) against the modulation index values (y-axis) for linearly modulated voxels. Boxplots plots indicate that the voxel-wise modulation index and minimum modeled activation values were significantly larger for fUSI than for fMRI (n = 7 animals, *** $p < 0.001$, Wilcoxon rank-sum test). Boxplots show the median (center line), $25^{th}$ and $75^{th}$ percentiles (boxes) and the $1^{st}$ and $99^{th}$ percentile (whiskers).

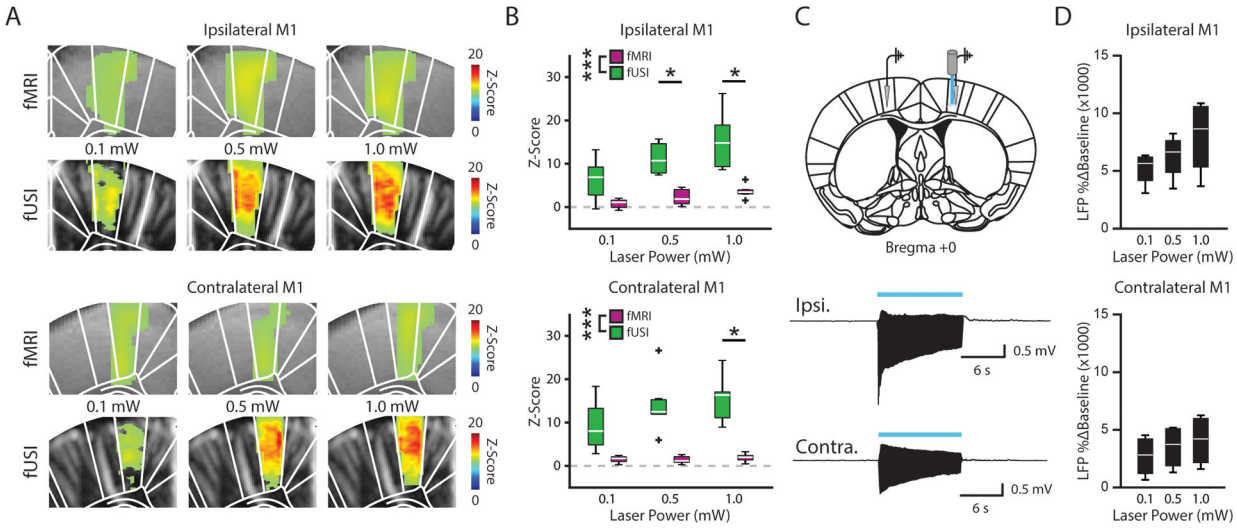


**Figure 3. Evoked M1 fUSI responses co-localize with the underlying neuronal activity.**

(**A**) Functional MRI and fUSI time series were converted to z-scores using a 30 second pre-stimulation baseline. Voxel-wise maps for the ipsilateral (top) and contralateral (bottom) M1 revealed an increase in the z-score of the evoked response across stimulation intensities for both fMRI and fUSI. (**B**) The average z-score during stimulation was significantly larger for fUSI (green) than for fMRI (purple) in the bilateral M1 (n = 4 animals, *** $p < 0.005$, two-way ANOVA, * $p < 0.05$, Tukey's HSD post hoc). **(C)** Local field potentials (LFP) were recorded from the ipsilateral (top trace) and contralateral M1 (bottom trace) (n = 4 mice) in response to optogenetic stimulations. (**D**) LFP response amplitude (% Δ Baseline) increased with stronger stimulation intensities in the bilateral M1. Boxplots in B and D show the median (center line), 25$^{th}$ and 75$^{th}$ percentiles (boxes) and the 1$^{st}$ and 99$^{th}$ percentile (whiskers).

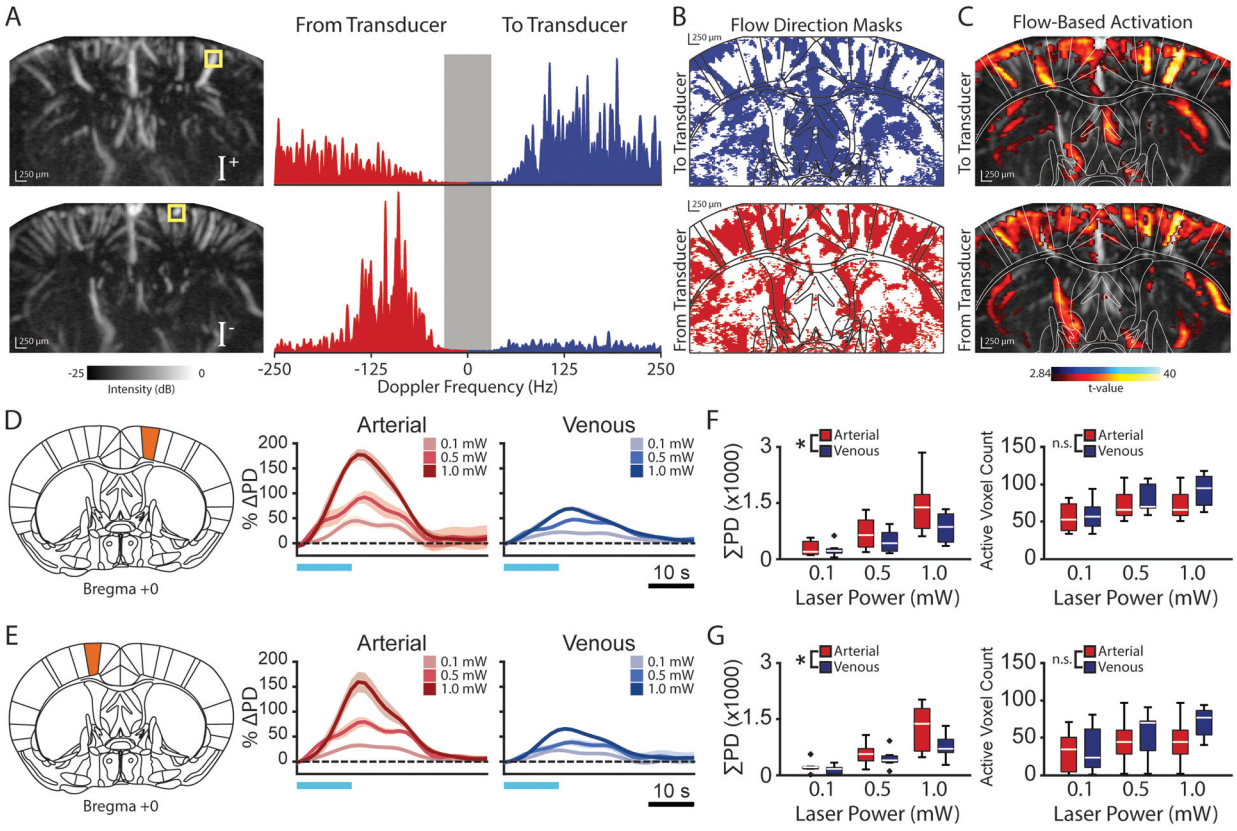


**Figure 4. Functional ultrasound imaging reveals vessel-specific hemodynamic responses to optogenetic stimulation.**

**(A)** Positive ($I^+$, top) and negative ($I^-$) power Doppler (PD) spectrum images indicate blood flow to and from the transducer, respectively. Example power spectra from individual voxels (yellow box) containing blood flowing towards (top) and away from (bottom) the transducer. Tissue content (<30 Hz) is removed from the PD image. **(B)** Blood flow direction masks were generated for each animal by assigning a binary direction to each voxel based on the stronger portion (positive or negative) of its power spectrum. **(C)** Blood flow direction masks were then applied to the activation maps of the corresponding animal to identify activated voxels in which blood flowed towards and away from the transducer. **(D–E)** Representative estimated average single-cycle arterial and venous evoked activity (%ΔPD) in response to varying levels of optogenetic stimulation in the ipsilateral **(D)** and contralateral **(E)** primary motor cortex (M1). Data are presented as mean (color) ± SEM (shaded region). Horizontal blue lines indicate the stimulation period. **(F–G)** The area under the response curve (ΣPD) is significantly larger for arterioles (red) than for venules (blue) in the ipsilateral **(F)** and contralateral **(G)** M1 despite a similar number voxels being activated (n = 7 animals, * $p < 0.05$, two-way ANOVA). Boxplots in F and G show the median (center line), 25$^{th}$ and 75$^{th}$ percentiles (boxes) and the 1$^{st}$ and 99$^{th}$ percentile (whiskers).